Energy 267 (2023) 126620

Contents lists available at ScienceDirect

Energy

journal homepage: www.elsevier.com/locate/energy

Investigation of premixed hydrogen/methane flame propagation and kinetic characteristics for continuous obstacles with gradient barrier ratio

Shuo Wang [a], Guoqing Xiao [a,b,*], Yu Feng [c], Hongfu Mi [d,**]

[a] College of Chemistry and Chemical Engineering, Southwest Petroleum University, Chengdu, 610500, PR China
[b] Oil & Gas Fire Protection Key Laboratory of Sichuan Province, Chengdu, Sichuan, 611731, PR China
[c] School of Chemical Engineering, Oklahoma State University, Stillwater, OK, 74078, USA
[d] College of Safety Engineering, Chongqing University of Science and Technology, Chongqing, 401331, PR China

ARTICLE INFO

Handling Editor: Wojciech Stanek

Keywords:
Premixed explosion
Gradient obstacles
Simulation flame
Explosion dynamics
Vortices

ABSTRACT

Employing both experimental and computational methods, this paper investigates the propagation characteristics of the explosion flame for two cases with gradually increasing and decreasing barrier ratios of continuous obstacles. Three variation gradients of barrier ratio were set in the increasing and decreasing continuous obstacle regions (i.e., 0.1, 0.2, and 0.3). Experimental results show that the flame front is less prone to inversion. With the increase in the barrier ratio of continuous obstacles, the effectiveness of the flame front in counteracting the impact of inversion can be enhanced. However, the maximum flame speed corresponds to the moment delay. Obstacles with larger initial barrier ratios will induce higher flame speed. For explosive overpressure, the accumulation and superposition of precursor waves and expansion waves during the rapid release can generate higher overpressure downstream, with the increase in barrier ratio. Lower downstream overpressure is due to the weaker pressure accumulation efficiency with the decreasing barrier ratio. Numerical simulation results visualize the distribution of the vorticity behind the obstacle, which explicitly unveils the generation and evolution of vortices in space. The underlying mechanism of how the flame was squeezed and stratified is analyzed and discussed as well.

1. Introduction

In dealing with climate issues, nations and regions have proposed new energy development strategies. Since the Paris Agreement was signed, various nations have begun planning for the creation of a sustainable, low-carbon future [1–3]. Hydrogen is a new energy source due to its high combustion heat value, lightweight, and the fact that the combustion product only produces water [4,5]. As a topic highly related to the safety of living and production for economic and social development, safe energy management has been widely studied. For example, a severe explosion accident occurred at the Fukushima nuclear power plant induced by hydrogen gas leakage in 2011 [6,7]. Combustible gas explosion accidents in many countries are also one of the most serious safety production accidents [8–10]. Although hydrogen does not contaminate the environment when used directly as an energy source, its extremely large explosion range and high combustibility and flammability make it difficult to control in existing process conditions [11]. Moreover, as the lightest gas on earth, hydrogen imposes high demands on the control valve efficiency during storage and transportation [12]. Therefore, researchers propose adding hydrogen to methane to achieve a complementary gas mixture in performance and economics [13–17].

Previous studies have revealed that obstacles in space can trigger the explosion reaction process easily, resulting in faster flame propagation speed and higher overpressure. Kindracki et al. [18] demonstrated that the presence of an obstacle shortens the combustion time and increases the rate of pressure rise. Zhang et al. [19] identified that obstacles could increase the reaction rate. Consequently, when the barrier ratio reaches the critical value, the perturbation effect on the flame can be maximized, in which will lead to the highest turbulence intensity and explosive strength. Zhou et al. [20] proved that a sharper obstacle can trigger a more violent explosion. The most dangerous explosions occur when the distance between the obstacles is almost equal to the inner diameter of the tube. Xiao et al. [21] further demonstrated that obstacles with cusps promote the generation of flow instabilities and create more intense

* Corresponding author. College of Chemistry and Chemical Engineering, Southwest Petroleum University, Chengdu, 610500, PR China.
** Corresponding author.
E-mail addresses: xiao13541694312@163.com (G. Xiao), mimihh5@163.com (H. Mi).

https://doi.org/10.1016/j.energy.2023.126620
Received 2 September 2022; Received in revised form 2 January 2023; Accepted 3 January 2023
Available online 4 January 2023
0360-5442/

flame-burning behavior. Qin et al. [22] indicated that the propagation of explosion flames in obstacle conditions is consistent with self-similarity. The Kelvin-Helmholtz instability and Rayleigh-Taylor instability caused by the obstacle generate significant flame stretching, which increases the turbulence of the flame. Zhou et al. [23] demonstrated that the flame acceleration of the explosion is attributed to the mutual promotion of flame instability and turbulence caused by the obstacle. However, the effect of the built-in obstacle on the maximum flame front speed is relatively limited [24]. Pang et al. [25] investigated by numerical simulation and found that the obstacle caused severe deformation of the explosion flame in space and destroyed the shape of the external flame. Cao et al. [26] found that obstacles can affect the flame propagation process by changing the flame structure, which in turn indirectly affects the flame speed and explosion intensity. Yang et al. [27] found that vortex motion due to obstacles is the primary mechanism of flame deformation, which resulted in a new pattern of tulip flame development. Na'inna et al. [28,29] showed that maximum overpressure is achieved at 2.25 m obstacle separation using a single flat-bar obstacle. Lv et al. [30] showed that the maximum peak overpressure occurs in the downstream region of the farthest obstacle position. Wen et al. [31] demonstrated that flame speed and peak overpressure increased with the number of obstacles, while the time to peak cannot be completely determined. Ago et al. [32] proved that the flame is greatly disturbed in a channel filled with repetitive obstacles, and the flame is accelerated by repeated local explosions, compression, and expansion in the flow path.

Partial studies have been conducted on the behavioral characteristics of gas explosions in obstacle conditions. It is worth noting that whether a single obstacle or multiple groups of obstacles were involved in previous studies controlled for a fixed barrier ratio. Currently, there is a lack of relevant studies on how the variation barrier ratio of continuous obstacles can impact gas explosion behaviors. The flame propagation behavior and dynamics characteristics in the explosion reaction should be investigated in detail when the barrier ratio of the continuous obstacle shows a gradient variation. Based on previous gas explosion studies, this paper investigated the effect of barrier ratio for gradient variation on explosion parameters with the hydrogen/methane mixture. This study is of great significance since (1) it fills knowledge gap on the effect of continuous gradient obstacles on gas explosions, and (2) it provides quantitative evidence as a guidance for safety and site design optimization for combustible gas fuels.

2. Experimental setup

Experiments were performed on a self-designed and built platform of mixed fuel explosion. The experimental setup of each system is shown in Fig. 1, including a premixed gas distribution system, a high-frequency ignition system, a high-frequency pressure acquisition system, and a fast image photographing system. The premixed gas distribution system included a hydrogen storage cylinder (purity 99.99%) and a methane storage cylinder (purity 99.99%). The combustion-supporting air was pre-stored by an air compressor. The premixed fuel equivalent ratio was 1.0, and the hydrogen content was 20 vol% in mixture fuel, because the equivalent ratio corresponds to the most visible explosion characteristics and 20 vol% hydrogen blending had already been used in existing energy devices [33–35]. The premixed gas was delivered to the explosion pipe via three ALICAT gas mass flowmeters. The explosion pipe is made of Plexiglas, with a size of 600 mm × 80 mm × 80 mm and a maximum withstanding pressure of 1.5 MPa. The left wall of the pipe was connected to a high-frequency pulse ignition device, which consisted of two disconnected metallic platinum wires that were energized to produce an electric spark to ignite the premixed fuel. The high-frequency pressure acquisition system consisted of a PCB sensor and a signal converter (Blast-PRO, designed by Chengdu Tytest). The sampling frequency is 125 kHz. The dynamic image photography system consisted of the Phantom VEO 710 L and a computer. The sampling frequency was 2000 fps, and the exposure time was 490 μs.

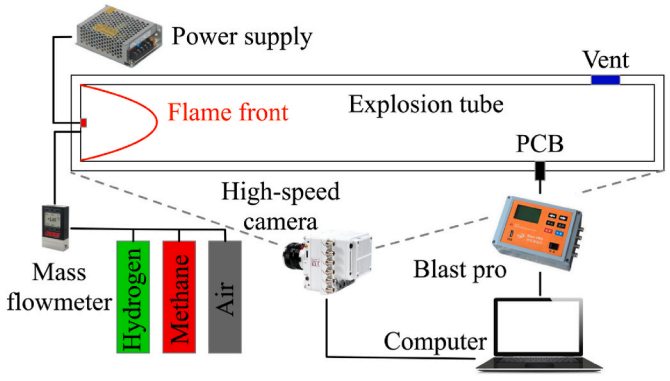

Fig. 1. Schematic diagram of the experimental system.

Fig. 2 presents the schematic diagram of the gradient barrier ratio (Definition: the ratio of the barrier area to the cross-sectional area of the pipe, $A_{barrier}/A_{pipe}$) for continuous obstacles, divided into continuous obstacle barrier increase (CBI) and continuous obstacle barrier decrease (CBD). The location of the obstacle was 100 mm (L-1), 200 mm (L-2), and 300 mm (L-3) from the ignition. With the gradually increasing barrier ratio, the initial barrier ratio was 0.2 at L-1 and the subsequent variations of the barrier are ΔCBI = 0.1, ΔCBI = 0.2, and ΔCBI = 0.3. The barrier ratio decreased gradually with an initial value of 0.8 at L-1, followed by decreasing cases of ΔCBD = −0.3, ΔCBD = −0.2, and ΔCBD = −0.1. A summary of the obstacle barrier ratios can be found in Table 1.

3. Numerical simulation setup

A two-dimensional planar model of 600 mm × 80 mm was built to simulate the premixed explosion reaction. A total of three groups of symmetrical continuous gradient obstacles were set at 100 mm intervals in the model. The barrier ratio of the obstacle was kept consistent with Table 1 and a 1.0-mm structured mesh was used for calculation.

The premixed gas explosion reaction is a complex phenomenon involving chemical kinetics, heat transfer, and fluid dynamics. The governing equations, i.e., conservation laws of mass, momentum, and energy, as well as the ideal gas law, are listed below [36–39].

$$\frac{\partial \rho}{\partial t}+\frac{\partial}{\partial x_i}(\rho u_i)=0 \tag{1}$$

$$\frac{\partial}{\partial t}(\rho u_i)+\frac{\partial}{\partial x_i}\left(\rho u_i u_j\right)=-\frac{\partial P}{\partial x_i}+\frac{\partial \sigma_{ij}}{\partial x_j} \tag{2}$$

$$\frac{\partial}{\partial t}(\rho e)+\frac{\partial}{\partial x_i}\left(u_i(\rho e+P)\right)=\frac{\partial}{\partial x_i}\left(k_{eff}\frac{\partial T}{\partial x_i}-\sum h_m J_m+u_j\sigma_{ij}\right)+\dot{Q}_c \tag{3}$$

$$\frac{\partial}{\partial t}(\rho Y_m)+\frac{\partial}{\partial x_i}(\rho u_i Y_m)=\frac{\partial}{\partial x_i}\left(\rho D_m\frac{\partial Y_m}{\partial x_i}\right)+\dot{\omega}_m \tag{4}$$

$$\sigma_{ij}=\mu\left(\frac{\partial u_i}{\partial x_j}+\frac{\partial u_j}{\partial x_i}\right)-\frac{2}{3}\mu\frac{\partial u_i}{\partial x_i}\delta_{ij} \tag{5}$$

$$P=\rho RT \tag{6}$$

where ρ is the density (kg/m^3), t is the time (s), x_i is spatial coordinates in the ith direction, u_i is the flow velocity in the ith direction (m/s), σ_{ij} is the stress tensor (Pa), P is the pressure (Pa), k_{eff} is the coefficient of heat conduction (W/mK), $\dot{Q}_c$ is the heat source released by chemical reactions, and $e=-p/\rho+v_i^2/2$ is the internal energy. D_m, Y_m, h_m, $\dot{\omega}_m$ and J_m is the diffusivity coefficient, mass fraction, specific enthalpy, reaction rate and diffusion flux of species, respectivly. μ is the turbulence

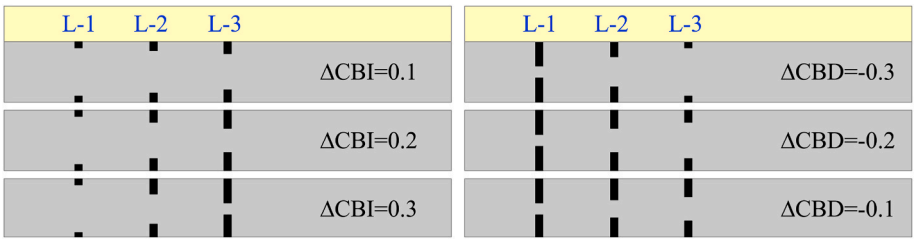

Fig. 2. Schematic diagram of obstacles barrier ratio.

Table 1
Continuous obstacle barrier ratio variables.

Continuous obstacle barrier increase (ΔCBI)				
Case number	Barrier ratio			Barrier ratio variable
	L-1	L-2	L-3	
Case1	0.2	0.3	0.4	ΔCBI = 0.1
Case2	0.2	0.4	0.6	ΔCBI = 0.2
Case3	0.2	0.5	0.8	ΔCBI = 0.3
Continuous obstacle barrier decrease (ΔCBD)				
Case number	Barrier ratio			Barrier ratio variable
	L-1	L-2	L-3	
Case4	0.8	0.5	0.2	ΔCBD = −0.3
Case5	0.8	0.6	0.4	ΔCBD = −0.2
Case6	0.8	0.7	0.6	ΔCBD = −0.1

viscosity coefficient, δ_{ij} is the Kronecker delta, R is the gas constant, T is the temperature (K).

Numerical simulations were performed in Ansys Fluent 2021. Specifically, the Renormalization Group (RNG) k-ε model was employed to model the turbulence. Compared with other Reynolds-Averaged Navier-Stokes (RANS) models (e.g., the standard k-ε model [39]), the RNG k-ε model can provide more accurate predictions in transient turbulent flow and flow bending. The mixed fuel explosion was adopted from the EDC model [40]. The thermal conductivity and dynamic viscosity of each component were calculated separately using the kinetic theory and Sutherland's formula [41,42]. The SIMPLE solver was used to decouple the velocity and pressure. To accurately capture the flame variation in the explosion pipe, the time step is determined by satisfying the condition that the Courant-Friedrichs-Lewy (CFL) number is less than 0.5. For convergence criteria, the residuals for mass, momentum, and energy equations are required to be lower than 1×10^{-5}, 1×10^{-5}, and 1×10^{-6}, respectively.

4. Results and discussion

4.1. Experimental measurements of the flame propagation process

Fig. 3 shows the propagation of the premixed flame at ΔCBI = 0.1. The acceleration of thermal diffusion [22] of the flame in the spherical and finger phases makes a clear demarcation between the flame and the unburned (between 6.0 ms and 15.0 ms). The flame passes into the CBI zone in a laminar state (between 18.0 ms and 22.0 ms). Due to the small barrier ratio of the initial obstacles, the disturbance to the flame precursor flow is weak, and the flame does not deform significantly after passing through the initial obstacles and still propagates with the finger shape. As the barrier ratio of obstacle increases, the flowing shear layer generates greater inertial forces in bypassing the obstacles, thus creating a pressure region between the obstacles and the flame [43]. At this point, the flame is subjected to a more pronounced squeezing phenomenon (t = 24.0 ms). The compression of the shear layer on the flame causes the flame to expand rapidly after passing through the obstacles. The flame boundary starts to curl and wrinkle, which is attributed to the Kelvin-Helmholtz instability formed at the flame boundary, disrupting the smooth flow. The turbulent flow disrupts the smooth flame boundary when the flame touches the unburned zone (t = 28.0 ms). The tendency of the flame structure to lose stability under continuous compression of the obstacles gradually increases. The feedback effect of the flow instability on the flame will be more significant than the flame thermal diffusion. After the flame passes through the CBI zone, the flame front is the first to expand compared to the flame stem, which forms a classic mushroom-shaped flame (between 29.0 ms and 29.5 ms) [22]. During the inversion of flame front, significant turbulent disturbances occurred near the boundaries of both the flame front and the flame stem. Based on the barometric pressure term of the vortex equation [44] ($\nabla P \times \nabla \rho / \rho^2$), the Rayleigh-Taylor instability occurs when the pressure and density gradients are not in the same direction, and the flame front transforms into a tulip structure (i.e., between 32.0 ms and 33.0 ms) with the effect of the continuous strengthening of the Rayleigh-Taylor instability in the subsequent propagation. Then, a wrinkled tulip flame front

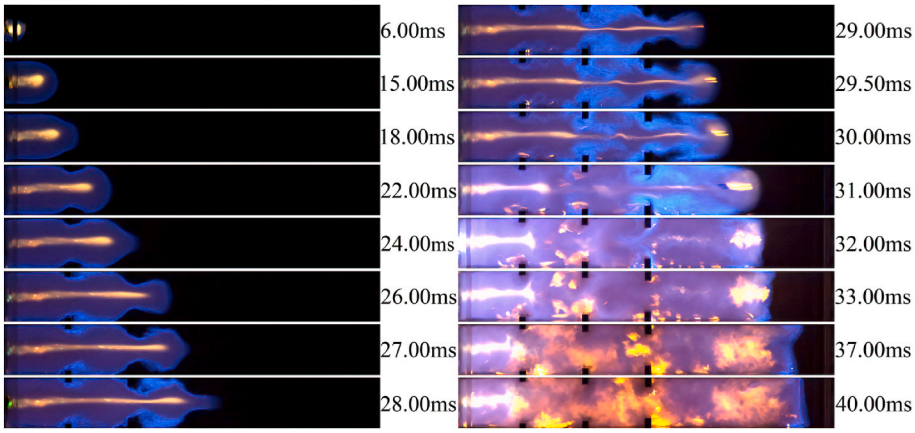

Fig. 3. Snapshot of the flame passing through the ΔCBI = 0.1 zone.

accompanied by a cellular structure was formed at the tongue of flame at t = 37.0 ms [12]. When the flame instability diminishes, the cellular structure gradually weakens, and the flame becomes smoother.

The flame propagation is visualized in Fig. 4 for ΔCBI = 0.2. The propagation of the flame within the CBI zone is significantly altered. When passing through the second obstacle zone, the expansion of the flame front is subjected to a more substantial feedback effect from the top and bottom walls. It is shown that the increase in the obstacle gradient can lead to an increase of the flow between obstacles disturbed by expansion waves. This is mainly reflected by the turbulent fluidization behavior of the unburned gas flow accumulating in the local space without timely dissipation. Before the flame passes into the high barrier ratio obstacles, the reverse expansion wave can briefly "flatten" the flame front. In this process of pressure waves continuously passing over the flame boundary, the flow instability increases the area of flame disturbance, and the degree of disturbance is more significant (i.e., between 25.0 ms and 26.0 ms). The flame is compressed once again after expansion and passes through the obstacles with pressure disturbance, the flame stem and front are stretched to an increased extent. This resulted in a slower burning behavior of the flame than the forward advance of the flame front. Delayed combustion occurred behind the flame front [45]. The flame expands outward at the front and at the stem simultaneously. It can be clearly observed that the flame has two regions of intense burning (i.e., between 27.0 ms and 28.0 ms). The flame boundary is disturbed by the more turbulent unburned gas, which increases the degree of flame wrinkles.

For ΔCBI = 0.3, the flame dynamic propagation process is shown in Fig. 5. The restricted area between the obstacles is again less efficient for releasing the disturbance when the flame passes through the second obstacle. The flame is compressed near the channel of obstacles by the pressure region formed from the shear layer, and the flame longitudinal spreading ability is further reduced. The Kelvin-Helmholtz instability due to shear layer shedding causes the flame boundary to recoil severely. The combined effect of perturbation and compression in the obstacle recirculation zone causes the flame stem to be almost truncated (i.e., between 25.0 ms and 26.0 ms). As the barrier ratio increases, the flame front gradually increases larger than the original main part when the reversal skirt occurs in the obstacles zone. This results in a turbulent combustion behavior that will take place simultaneously in multiple locations. This phenomenon occurs more obviously after the flame has passed through the CBI zone (i.e., between 26.5 ms and 27.0 ms). The flame is driven by the high-speed flow to complete the turbulence maximization faster. The increase in turbulence intensity will result in wrinkling of the flame boundary during expansion, and the increased degree of flame wrinkling contributes to the development of flame turbulence. Thus, flame wrinkles and turbulent perturbations both provide positive feedback to each other, which improves the ability of the flame to counteract reflected waves, and results in a reduced tendency for the flame to be canceled. The confrontation between the flame and the reflected wave remains even when the flame is close to the wall at the end of its propagation. The local projection of the flame front before the transition to the quasi-plane indicates that the flame still has a strong propulsive tendency.

The flame is initially squeezed and deformed when passing through the CBD zone, as shown in Fig. 6. The spherical flame then develops into a finger flame in laminar combustion with free expansion [22]. When the flame front is close to the obstacle, the pressure region around the obstacle squeezes the flame front into the CBD zone. Due to the high initial barrier ratio, the flame is stretched longer (t = 16 ms), driven by the high-speed compressed flow. It is worth mentioning that the flame boundary in the adjacent obstacle interval produces a layered Kelvin-Helmholtz instability during the expansion at t = 17 ms–20 ms, and the flame boundary is stretched and curled. From the flame front to the flame stem, the newly curled flame is within the range of the previous curled flame (i.e., between 17.0 ms and 18.5 ms). Local instability arises in a large-scale instability, and this effect causes the flame to be accelerated forward layer by layer. The pressure region between the flame and the obstacle decreases, and the reduced shear layer stretching weakens the effect of flame disturbance [46] in the CBD zone. As a result, the proportion of curled flame skirt decreased, and the inward of the tulip flame at the end propagation is significant.

With the further increase in the barrier ratio of the CBD, the flame skirt is more susceptible to curl by the Kelvin-Helmholtz instability, as shown in Fig. 7. The ability of the flame to advance forward is increased. However, it is still possible to form a tulip flame. It is worth mentioning that the degree of the tulip flame inward is reduced.

In Fig. 8, when ΔCBD = −0.1, the flame forms an umbrella structure as it passes through the obstacles zone. The Kelvin-Helmholtz instability, the flame is affected in the obstacles zone leading to a chaotic burning boundary. As the ΔCBD increases, the relative stability of the flame center decreases. The erosive effect of the chaotic zone on the flame is then enhanced (t = 19.0 ms). Although the flame remains in finger shape for a more extended period, it eventually forms a tulip flame. It is shown that the CBD zone is not conducive to the flame against the inversion in the propagation.

4.2. Experimental measurements of the flame propagation speed

Fig. 9 provides the variation of flame front speed with the position in the pipe over time. The position (x_F) and speed (v_F) of the flame front is tracked from the image sequence by pixel displacement and time (t) interval information of the flame front [46]. v_F can be calculated by

$$v_F = \frac{x_F(t+\Delta t) - x_F(t)}{\Delta t} \tag{7}$$

In Fig. 9 (a)–(f) corresponding to Cases 1 to 6 (in Table 1) respectively, the obstacles have negligible effect on the flame front speed until it reaches the 100 mm obstacle zone. The thermal diffusion mainly dominates the flame before it reaches the obstacle area [22]. The compression wave generated by the expanding gas does not contribute significantly to the flame speed. Then, the flame has a significant acceleration in the obstacle zone, which expands and pushes the unburned

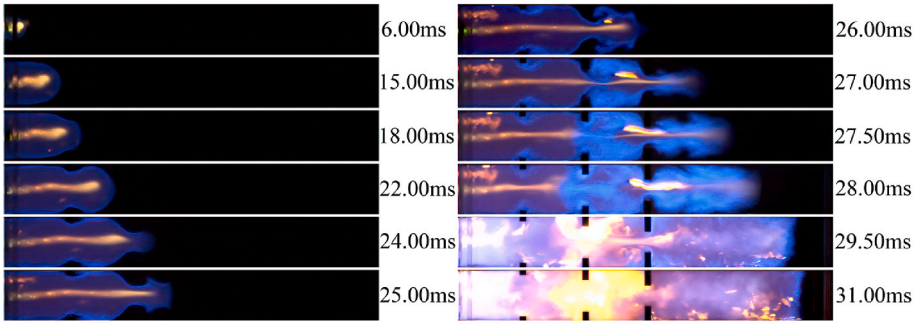

Fig. 4. Snapshot of the flame passing through the ΔCBI = 0.2 zone.

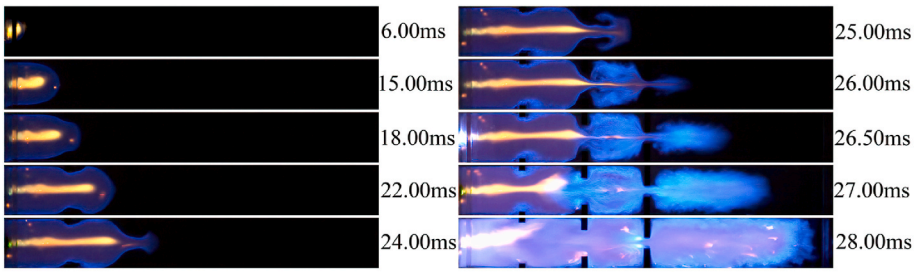

Fig. 5. Snapshot of the flame passing through the ΔCBI = 0.3 zone.

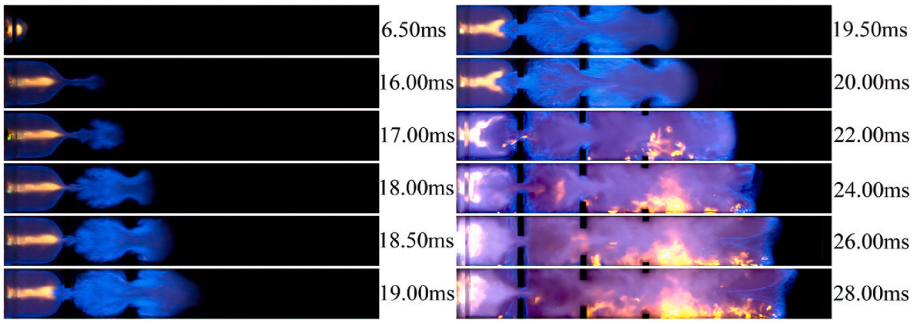

Fig. 6. Snapshot of the flame passing through the ΔCBD = −0.3 zone.

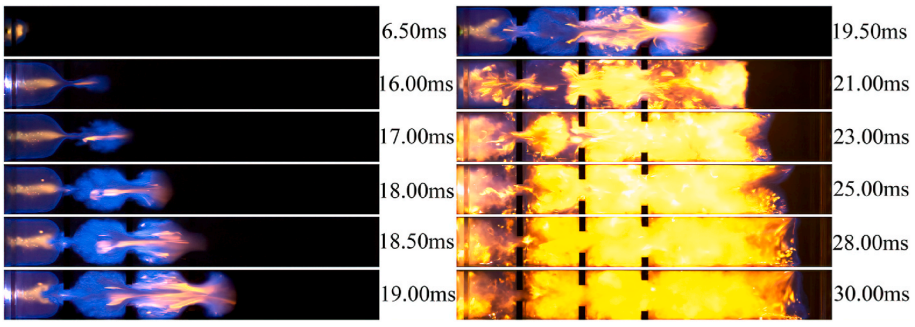

Fig. 7. Snapshot of the flame passing through the ΔCBD = −0.2.

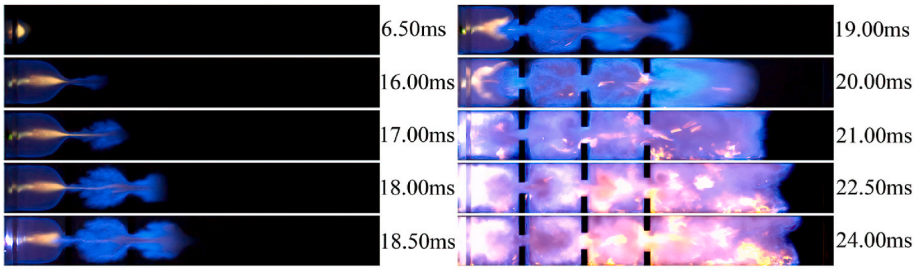

Fig. 8. Snapshot of the flame passing through the ΔCBD = −0.1.

gas to the flame front, driving the flame front to propagate. Simultaneously, the recirculation zone behind the obstacle stretches the flame boundary, increasing the contact area with the mixture and increasing the flame speed by enhancing the combustion efficiency (according above flame propagation in Figs. 3–8).

The delayed combustion of the flame stem provides advancing assistance to the front after the flame passes through the obstacles [47], when the continuous obstacle barrier ratio is gradually increased in Fig. 9 (a)–(c) corresponding to Cases 1 to 3. Increased ΔCBI can cause the flame front to maintain its forward propulsive behavior without decay after passing through the obstacles. The maximum speed that the flame front can reach with Cases 1 to 3 are 52.17 m/s, 88.00 m/s, and 128.00 m/s, respectively. The flame front speed is changed in Fig. 9 (d)–(f) corresponding to Cases 4 to 6. The flames accelerate earlier and faster into the acceleration stage. However, after the flame fronts entered the obstacles zone, the flame fronts all generated a brief decrease. Combined with the analysis shown in Figs. 6–8, it can be found that a large barrier ratio of the L-1 obstacle can suddenly elongate the turbulent boundary of the flame to increase the flame speed in the obstacle region. However, this turbulent boundary is difficult to maintain with a small barrier ratio.

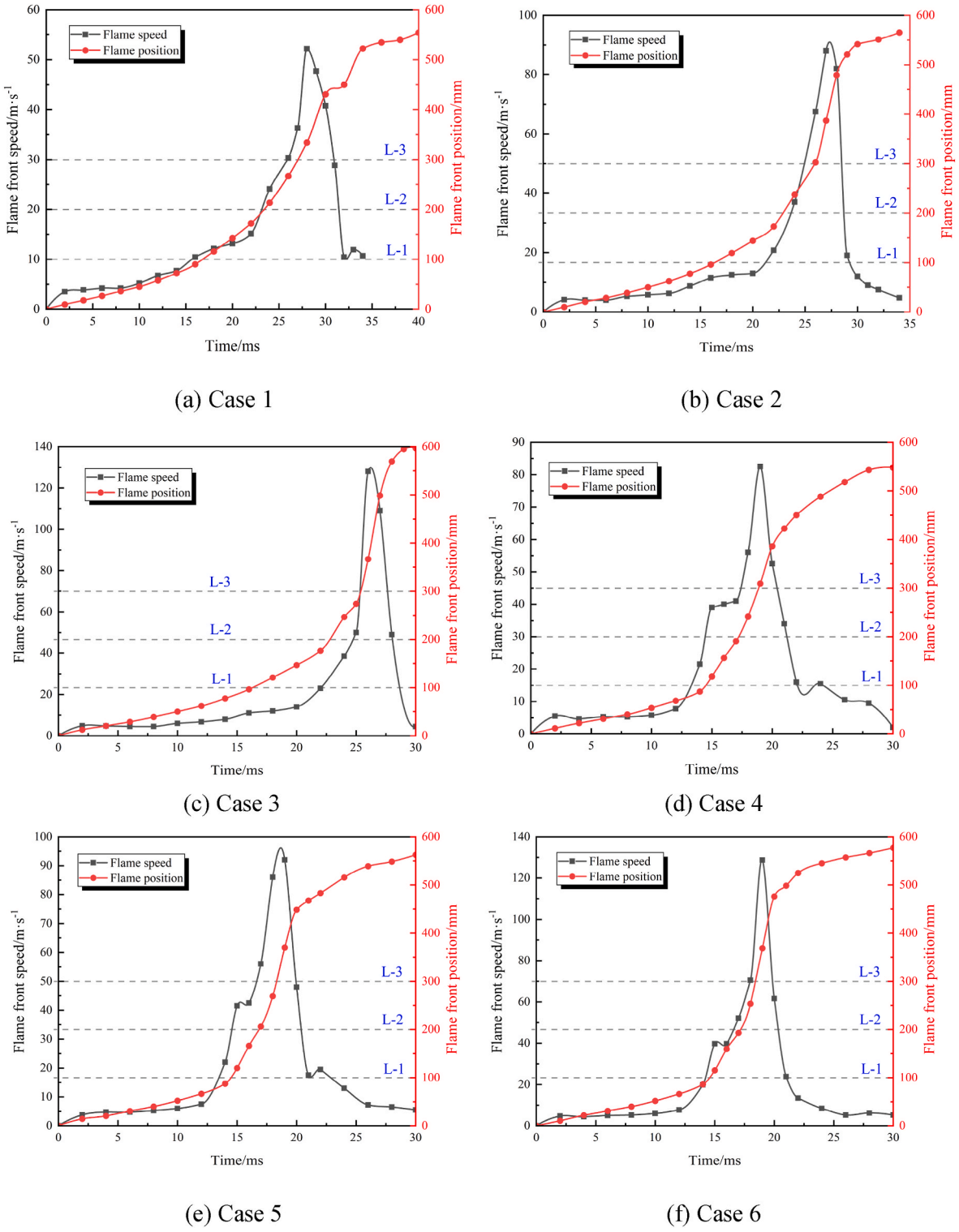

Fig. 9. Relationship between the speed and position of the flame front with time.

Additionally, the flame diffusion to the wall weakens the forward-pushing behavior of the flame front. Such an effect is improved with the increased barrier ratio. The maximum speed that the flame can reach is 82.50 m/s, 92.00 m/s, and 128.70 m/s by the obstacles, respectively. The sudden increase in the speed of the flame front will temporarily decrease in the process, but as the flame instability increases, the maximum speed of the flame being excited is higher than the original gradual increase in the speed of the flame. Therefore, in the condition of multiple groups of continuous obstacles, the maximum value of flame front speed is determined by all obstacles together, but the position corresponding to the maximum value is determined by the obstacle with the largest barrier ratio.

4.3. Experimental measurements on the variation of the explosion pressure

As the continuous barrier ratio changes, the overpressure downstream of the obstacle changes with time. It can be seen in Fig. 10 (a) that there is a significant contribution to the downstream overpressure when the continuous barrier ratio gradually increases. The increase in maximum overpressure is accompanied by an earlier moment of overpressure rise. The maximum overpressure at ΔCBI = 0.2 increased by 109.18 kPa compared to ΔCBI = 0.1. The maximum overpressure at ΔCBI = 0.3 increased by 120.76 kPa compared to ΔCBI = 0.2. The difference between the maximum overpressure is gradually increasing. However, it is noteworthy that the maximum overpressure of the CBD significantly decreases in Fig. 10 (b). Compared to Fig. 10 (a), the effect is weaker, although the difference between the maximum pressure is increased. The maximum pressure is enhanced by approximately 50.0 kPa. Meanwhile, the moment when the overpressure starts to rise is not distinguished in Fig. 10 (b).

The change rate of overpressure during the rise is obtained by linearly fitting the experimental data, as shown in Fig. 11. The rate of pressure increase is higher in continuous obstacles barrier ratio increase (see Fig. 11 (a)). When the explosion overpressure generates a higher rate of increase, it can often result in a higher pressure peak. The evidence indicates that pressure accumulation effects benefit pressure value increases [47]. For CBI, the gradual increase of the barrier influence causes an incremental accumulation of pressure in the obstacle interval, resulting in higher pressures during the pressure release period. For larger initial obstacle barrier ratios, as CBD case, the pressure has been released before adequate accumulation, a smaller downstream barrier ratio is not conducive to accumulating pressure waves resulting in a smaller total pressure maximum (see Fig. 11 (b)).

4.4. The effect of the flow velocity field on the flame

The developments of the streamlines in the obstacle space over time based on numerical simulations are presented in Figs. 12 and 13. For the numerical simulation results, the red in the figure represents the burnt region, the blue represents the unburned region, and the white arrows indicate the movement of the streamlines.

Fig. 12 shows the dynamics of the streamlines in the pipe during flame propagation for CBI. During flame development, the vortices corresponding to the size of the obstacle formed behind the obstacle. As time progresses, the vortices gradually expand in extent but disappeared due to the loss of dominance of spin caused by a decrease in speed gradient as the flame passes through the obstacles [39]. It is worth noting that the obstacle recirculation zone is accompanied by an increased barrier ratio, while the elongated shear layer by obstacle leads to greater vortices shedding [48,49]. At ΔCBI = 0.2, the vortices behind the third obstacle stretch into an elliptical structure, and the center of the vortices are displaced downstream away from the obstacles. The same phenomenon still occurs at ΔCBI = 0.3. While the vortices behind the obstacle are stretched, two new vortices generates behind the obstacle as the center of the first formed vortices move downstream. As a result, multiple vortices coexist in the elliptical region. Therefore, the flame boundary in the experiment is perturbed in multiple regions at this phase, triggering multiple wrinkles and curls in the flame. The elliptical vortices tend to separate the vortex region from the flame region through the shear layer, as the experimental results show, causing the initial flame to be compressed into a long strip shape and limiting the tendency of the flame to move in a longitudinal expansion.

Fig. 13 illustrates the vector streamlines variation in flame propagation with CBD. When the initial obstacle barrier ratio is large, the large-scale vortices are the first to form behind the obstacles, confining the flame to propagate within the channel of the obstacle. Since the boundary layer separation effect of the shear flow, the vortices region behind the obstacles forms a larger velocity gradient that the vortices are less prone to dissipation [50]. Therefore, the large size vortex does not dissipate immediately after the flame passes through the first obstacle, but instead, many small-scale vortices (Fig. 13 (a) t = 15.00 ms; Fig. 13 (b) t = 15.00 ms; Fig. 13 (c) t = 14.00 ms). When an individual vortex is strong enough, it does not immediately dissipate. The multiple small-scale vortex triggers the occurrence of experimental flame layering Kelvin-Helmholtz instability with stacking of flame front. Therefore, it can be inferred that the large-scale vortex in the explosion reaction causes the flame to deform and the small-scale vortex can increase the degree of wrinkling of the flame front and enhance the mixing behavior of the flame boundary with the mixture gas. In the case of CBD, the downstream obstacles have a weaker compression behavior on the flame due to the smaller barrier ratio, leading to a more rapid reduction or disappearance of the vortices.

4.5. Effect of vorticity field on flame

Figs. 14 and 15 shows the variation of the vorticity field obtained from the numerical simulation results. The green in the figure represents the region where the vorticity is 0. The red represents the positive

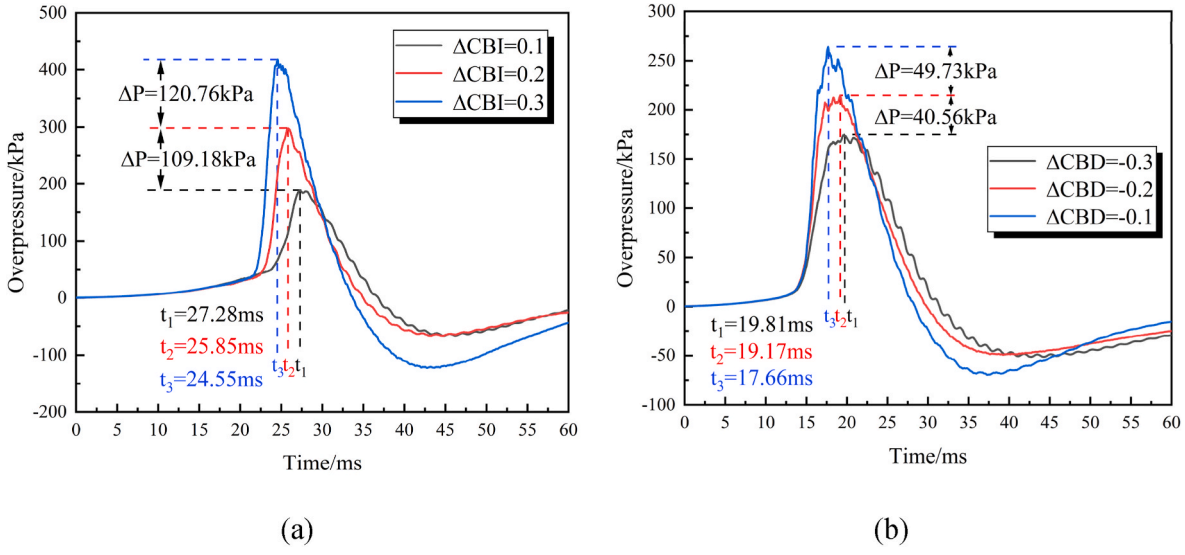

Fig. 10. Explosion overpressure development law with time.

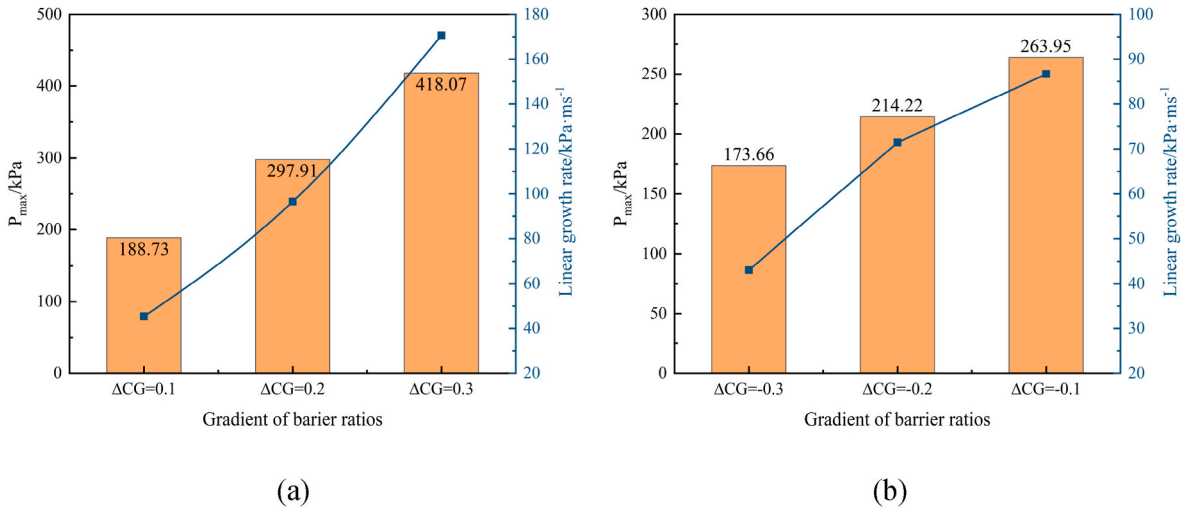

Fig. 11. Relationship between overpressure rise rate and maximum overpressure.

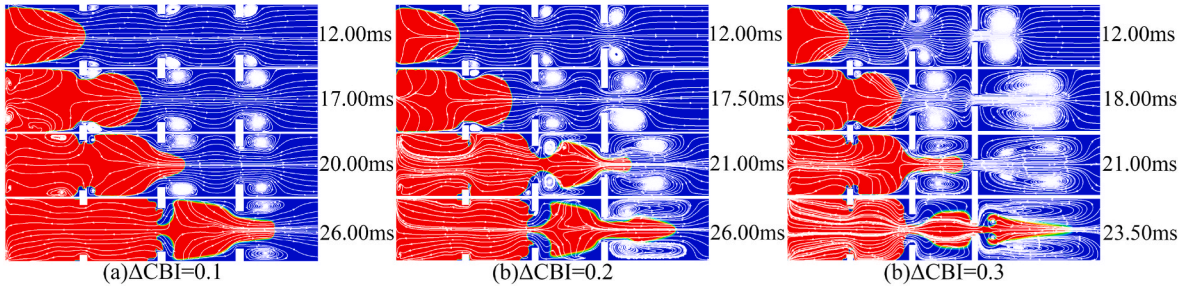

Fig. 12. Streamlines with increasing barrier ratio of continuous obstacles.

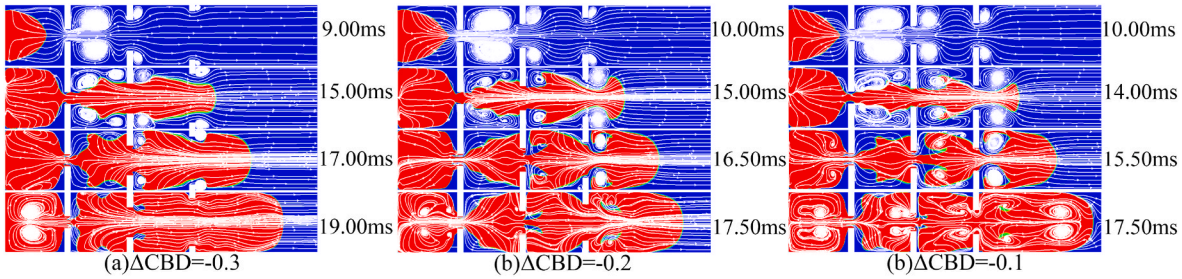

Fig. 13. Streamlines with decreasing barrier ratio of continuous obstacles.

vorticity forming at the top obstacle, and the blue represents the negative vorticity forming at the bottom obstacle. The darker the color, the greater the intensity.

Due to the presence of obstacles, the explosion reaction in the process of advancing must have been affected by the strain rate resulting in a velocity gradient. The distribution of vorticity can visually explain the causes and movement trends of vortex in space [39]. Fig. 14 provides the distribution of vorticity in space for CBI. It can be found that the greater the barrier ratio, the greater the range of influence of the vorticity. The deformation and distortion of the flame are all present in the region of larger vorticity. As the flame progresses, the vorticity dissipates at the obstacle and propagates along with the flame front. Both the top and bottom flame boundaries benefit from their respective expansions in response to different vorticity fields. For ΔCBI = 0.2 and ΔCBI = 0.3, the stretching and displacement downstream of the vorticity field interpret the trend of the vortex.

Fig. 15 shows the variation of vorticity with time for CBD. In Fig. 14, it is found that the vorticity in the continuous obstacle interval is independent of each other. In contrast, in Fig. 15, the obstacle with a larger initial barrier ratio leads to an elongation of the vorticity field and even has an impact on the formation and development of the vorticity field at the adjacent obstacles. The vorticity is continuous behind the obstacle with a large barrier ratio, and the velocity field is accompanied by the emergence of new spin regions to induce the vortices. Therefore, as the previous large-scale vortex dissipates to the small-scale, new vorticity fields create new vortices, which consequently generate multiple patterns in space. During each set of symmetric vortices shedding, the flame front curls and forms the stratified Kelvin-Helmholtz instability in the experiment. The evidence indicates that the pressure and speed change most intensely at the obstacle in the pipe [50]. Thus, larger barrier ratios of the L-1 obstacle can lead to higher initial vorticity. In the vortices flame and jet flame propagation phases, the vortices diffuse into the inside of the combustion products [50]. The larger initial vorticity accompanies the propagation of the flame, and the vorticity field reveals

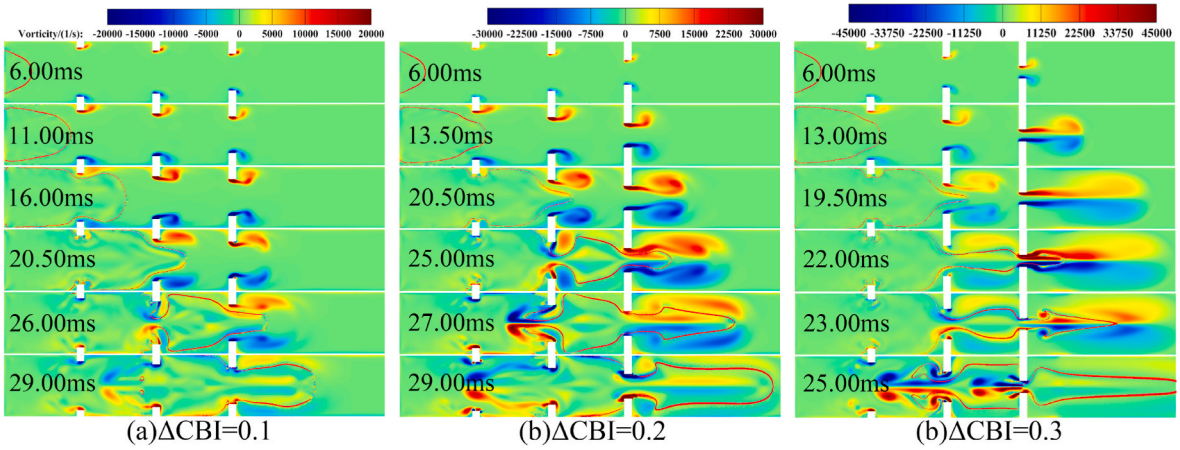

Fig. 14. Vorticity development with increasing barrier ratio of continuous obstacles.

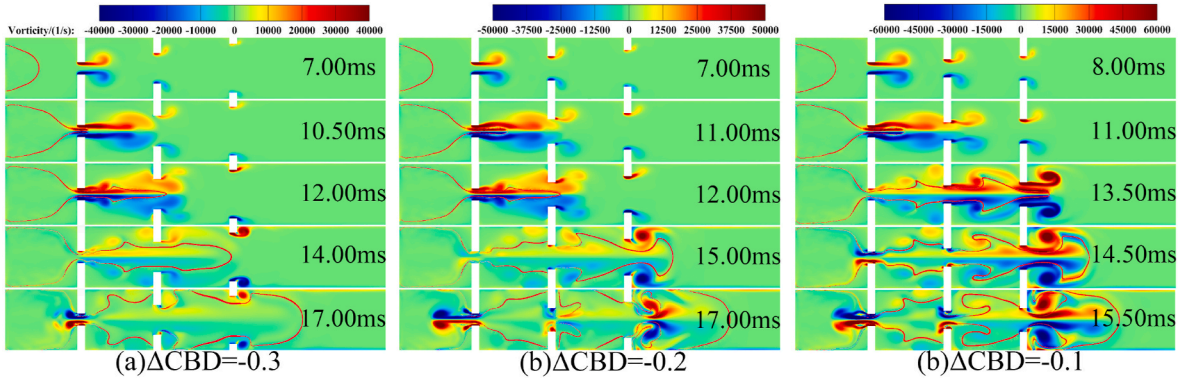

Fig. 15. Vorticity development with decreasing barrier ratio of continuous obstacles.

transferability. When the gradient of the barrier ratio decreases, the flame propagation induces intense pressure and speed changes in the obstacle increasing the transferability of the vorticity, so the vorticity downstream of the obstacle and in the pipe is more significant.

5. Conclusions

Employing both experimental and computational methods, this paper investigates the propagation characteristics of the explosion flame for two cases with gradually increasing and decreasing barrier ratios of continuous obstacles. Key conclusions are summarized below.

(1) When the barrier ratio of continuous obstacles increases, flame boundaries are more easily broken by turbulent flow in the downstream. When the continuous obstacle barrier ratio decreases, the flame is subjected to strong Kelvin-Helmholtz instability initially and generates a stratified curl. Flame is more conducive to counteracting inversion with increasing continuous barrier ratio and delaying the transition to flat structure but tends to inversion during a barrier ratio decrease.
(2) The flame speed is driven by the high-speed flow in addition to the gradual expansion after passing through the increasing barrier ratio. However, in the decreased gradient of barrier ratio, the flame speed originates more from the turbulence caused by the initial obstacle.
(3) The flame can achieve a more noticeable pressure increase rate and maximum pressure value with the increased gradient of barrier ratio, and the increase rate of pressure is proportional to the maximum pressure. In decreased barrier ratio, the pressure releases instantly, but the weaker accumulation process results in low downstream pressure.
(4) The vortices behind the obstacle dominate the flame behavior. Large-scale vortices compress flame to deformation, and small-scale vortices changes the smooth boundary of flame and increases the mixing efficiency between the flame and the mixture to increase the combustion rate. The distribution of the vorticity field determines the tendency of the vortices.

Author statement

Shuo Wang: Conceptualization, Methodology, Software, Validation, Investigation, Data curation, Writing – original draft, Writing – review & editing. **Guoqing Xiao:** Resources, Writing – original draft, Writing – review & editing, Supervision, Project administration, Funding acquisition. **Yu Feng:** Software, Resources, Data curation, Writing – review & editing. **Hongfu Mi:** Resources, Data curation, Writing – review & editing, Supervision, Project administration, Funding acquisition.

Declaration of competing interest

The authors declare that they have no known competing financial interests or personal relationships that could have appeared to influence the work reported in this paper.

Data availability

No data was used for the research described in the article.

Acknowledgement

This work is supported by the National Natural Science Foundation of China (NSFC 51874255, 52174209, 52274177). Chongqing Key Laboratory of Fire and Explosion Safety (LQ21KFJJ08). The authors are grateful for the numerical simulation support from the Computational Biofluidics and Biomechanics Laboratory (CBBL) at Oklahoma State University, Stillwater, Oklahoma, USA.

References

[1] Saheb Y, Shnapp S, Johnson C. The Zero Energy concept: making the whole greater than the sum of the parts to meet the Paris Climate Agreement's objectives. Curr Opin Environ Sustain 2018;30:138–50. https://doi.org/10.1016/j.cosust.2018.04.014.
[2] Creti A, Nguyen DK. Energy and environment: transition models and new policy challenges in the post Paris Agreement. Energy Pol 2018;122:677–9. https://doi.org/10.1016/j.enpol.2018.07.048.
[3] Kuriakose J, Jones C, Anderson K, McLachlan C, Broderick J. What does the Paris climate change agreement mean for local policy? Downscaling the remaining global carbon budget to sub-national areas. Renewable and Sustainable Energy Transition 2022;2:100030. https://doi.org/10.1016/j.rset.2022.100030.
[4] Luo Z, Wang X, Wen H, Pei A. Hydrogen production from offshore wind power in South China. Int J Hydrogen Energy 2022. https://doi.org/10.1016/j.ijhydene.2022.03.162.
[5] Johnston C, Ali Khan MH, Amal R, Daiyan R, MacGill I. Shipping the sunshine: an open-source model for costing renewable hydrogen transport from Australia. Int J Hydrogen Energy 2022. https://doi.org/10.1016/j.ijhydene.2022.04.156.
[6] Fujisawa N, Liu S, Yamagata T. Numerical study on ignition and failure mechanisms of hydrogen explosion accident in Fukushima Daiichi Unit 1. Eng Fail Anal 2021;124:105388. https://doi.org/10.1016/j.engfailanal.2021.105388.
[7] Luangdilok W. The explosions at Fukushima Daiichi Unit 3 and Unit 4 and implications on the evaluation of 1F3 accident. Nucl Eng Des 2020;362:110536. https://doi.org/10.1016/j.nucengdes.2020.110536.
[8] Meng X, Liu Q, Luo X, Zhou X. Risk assessment of the unsafe behaviours of humans in fatal gas explosion accidents in China's underground coal mines. J Clean Prod 2019;210:970–6. https://doi.org/10.1016/j.jclepro.2018.11.067.
[9] He Z, Wu Q, Wen L, Fu G. A process mining approach to improve emergency rescue processes of fatal gas explosion accidents in Chinese coal mines. Saf Sci 2019;111:154–66. https://doi.org/10.1016/j.ssci.2018.07.006.
[10] Chunli Y, Xiangchun L, Yanbin R, Yiliang Z, Feifei Z. Statistical analysis and countermeasures of gas explosion accident in coal mines. Procedia Eng 2014;84:166–71. https://doi.org/10.1016/j.proeng.2014.10.422.
[11] Yu M, Zheng K, Zheng L, Chu T, Guo P. Effects of hydrogen addition on propagation characteristics of premixed methane/air flames. J Loss Prev Process Ind 2015;34:1–9. https://doi.org/10.1016/j.jlp.2015.01.017.
[12] Zheng K, Yu M, Zheng L, Wen X. Comparative study of the propagation of methane/air and hydrogen/air flames in a duct using large eddy simulation. Process Saf Environ Protect 2018;120:45–56. https://doi.org/10.1016/j.psep.2018.08.025.
[13] Zheng K, Yu M, Zheng L, Wen X, Chu T, Wang L. Experimental study on premixed flame propagation of hydrogen/methane/air deflagration in closed ducts. Int J Hydrogen Energy 2017;42:5426–38. https://doi.org/10.1016/j.ijhydene.2016.10.106.
[14] Zheng K, Yu M, Liang Y, Zheng L, Wen X. Large eddy simulation of premixed hydrogen/methane/air flame propagation in a closed duct. Int J Hydrogen Energy 2018;43:3871–84. https://doi.org/10.1016/j.ijhydene.2018.01.045.
[15] Jin W, Ren C, Li J, Wang J, Yan Y. Experimental study on characteristics of CH4/H2 oxy-fuel turbulent premixed flames. Fuel 2022;310:122292. https://doi.org/10.1016/j.fuel.2021.122292.
[16] Wang T, Liang H, Lin J, Luo Z, Wen H, Cheng F, et al. The explosion thermal behavior of H2/CH4/air mixtures in a closed 20 L vessel. Int J Hydrogen Energy 2022;47:1390–400. https://doi.org/10.1016/j.ijhydene.2021.10.092.
[17] Berwal P, Solagar S, Kumar S. Experimental investigations on laminar burning velocity variation of CH4+H2+air mixtures at elevated temperatures. Int J Hydrogen Energy 2022;47:16686–97. https://doi.org/10.1016/j.ijhydene.2022.03.155.
[18] Kindracki J, Kobiera A, Rarata G, Wolanski P. Influence of ignition position and obstacles on explosion development in methane–air mixture in closed vessels. J Loss Prev Process Ind 2007;20:551–61. https://doi.org/10.1016/j.jlp.2007.05.010.
[19] Zhang K, Wang Z, Ni L, Cui Y, Zhen Y, Cui Y. Effect of one obstacle on methane–air explosion in linked vessels. Process Saf Environ Protect 2017;105:217–23. https://doi.org/10.1016/j.psep.2016.11.004.
[20] Zhou Y hui, shu Bi M, Qi F. Experimental research into effects of obstacle on methane-coal dust hybrid explosion. J Loss Prev Process Ind 2012;25:127–30. https://doi.org/10.1016/j.jlp.2011.07.003.
[21] Xiao G, Wang S, Mi H, Khan F. Analysis of obstacle shape on gas explosion characteristics. Process Saf Environ Protect 2022;161:78–87. https://doi.org/10.1016/j.psep.2022.03.019.
[22] Qin Y, Chen X. Flame propagation of premixed hydrogen-air explosion in a closed duct with obstacles. Int J Hydrogen Energy 2021;46:2684–701. https://doi.org/10.1016/j.ijhydene.2020.10.097.
[23] Zhou Y, Li Y, Jiang H, Huang L, Zhang K, Gao W. Experimental study on unconfined methane explosion: explosion characteristics and overpressure prediction method. J Loss Prev Process Ind 2021;69:104377. https://doi.org/10.1016/j.jlp.2020.104377.
[24] Li Y, Bi M, Zhou Y, Jiang H, Huang L, Zhang K, et al. Experimental and theoretical evaluation of hydrogen cloud explosion with built-in obstacles. Int J Hydrogen Energy 2020;45:28007–18. https://doi.org/10.1016/j.ijhydene.2020.07.067.
[25] Pang L, Jin M, Yang K. Effect of opening pressure and area blockage due to obstacles on vented natural gas explosion. J Eng Phys Thermophys 2022;95:142–51. https://doi.org/10.1007/s10891-022-02462-6.
[26] Cao X, Wei H, Wang Z, Wang Y, Fan L, Lu Y. Effect of obstacle on the H2/CO/Air explosion characteristics under lean-fuel conditions. Fuel 2022;319:123834. https://doi.org/10.1016/j.fuel.2022.123834.
[27] Yang X, Yu M, Zheng K, Luan P, Han S. An experimental study on premixed syngas/air flame propagating across an obstacle in closed duct. Fuel 2020;267:117200. https://doi.org/10.1016/j.fuel.2020.117200.
[28] Na'inna AM, Phylaktou HN, Andrews GE. Explosion flame acceleration over obstacles: effects of separation distance for a range of scales. Process Saf Environ Protect 2017;107:309–16. https://doi.org/10.1016/j.psep.2017.01.019.
[29] Na'inna AM, Phylaktou HN, Andrews GE. The acceleration of flames in tube explosions with two obstacles as a function of the obstacle separation distance. J Loss Prev Process Ind 2013;26:1597–603. https://doi.org/10.1016/j.jlp.2013.08.003.
[30] Lv X, Zheng L, Zhang Y, Yu M, Su Y. Combined effects of obstacle position and equivalence ratio on overpressure of premixed hydrogen–air explosion. Int J Hydrogen Energy 2016;41:17740–9. https://doi.org/10.1016/j.ijhydene.2016.07.263.
[31] Wen X, Yu M, Ji W, Yue M, Chen J. Methane-air explosion characteristics with different obstacle configurations. Int J Min Sci Technol 2015;25:213–8. https://doi.org/10.1016/j.ijmst.2015.02.008.
[32] Ago A, Tsuboi N, Dzieminska E, Hayashi AK. Two-dimensional numerical simulation of detonation transition with multi-step reaction model: effects of obstacle height. Combust Sci Technol 2019;191:659–75. https://doi.org/10.1080/00102202.2018.1498849.
[33] Isaac T. HyDeploy: the UK's first hydrogen blending deployment Project. Clean Energy 2019;3:114–25. https://doi.org/10.1093/ce/zkz006.
[34] Wen X, Wang M, Su T, Zhang S, Pan R, Ji W. Suppression effects of ultrafine water mist on hydrogen/methane mixture explosion in an obstructed chamber. Int J Hydrogen Energy 2019;44:32332–42. https://doi.org/10.1016/j.ijhydene.2019.10.110.
[35] Duan Y, Long F, Huang J, Jia H, Bu Y, Yu S. Effects of porous materials with different thickness and obstacle layout on methane/hydrogen mixture explosion with low hydrogen ratio. Int J Hydrogen Energy 2022;47:27237–49. https://doi.org/10.1016/j.ijhydene.2022.06.065.
[36] Xiao H, Sun J, Chen P. Experimental and numerical study of premixed hydrogen/air flame propagating in a combustion chamber. J Hazard Mater 2014;268:132–9. https://doi.org/10.1016/j.jhazmat.2013.12.060.
[37] Xiao H, Makarov D, Sun J, Molkov V. Experimental and numerical investigation of premixed flame propagation with distorted tulip shape in a closed duct. Combust Flame 2012;159:1523–38. https://doi.org/10.1016/j.combustflame.2011.12.003.
[38] Xiao H, Shen X, Sun J. Experimental study and three-dimensional simulation of premixed hydrogen/air flame propagation in a closed duct. Int J Hydrogen Energy 2012;37:11466–73. https://doi.org/10.1016/j.ijhydene.2012.05.006.
[39] Qin Y, Chen X. Study on the dynamic process of in-duct hydrogen-air explosion flame propagation under different blocking rates. Int J Hydrogen Energy 2022. https://doi.org/10.1016/j.ijhydene.2022.04.004.
[40] Shakeel MR, Sanusi YS, Mokheimer EMA. Numerical modeling of oxy-methane combustion in a model gas turbine combustor. Appl Energy 2018;228:68–81. https://doi.org/10.1016/j.apenergy.2018.06.071.
[41] Vanna F De, Picano F, Benini E. A sharp-interface immersed boundary method for moving objects in compressible viscous flows. Comput Fluids 2020;201:104415. https://doi.org/10.1016/j.compfluid.2019.104415.
[42] Xiao H, He X, Duan Q, Luo X, Sun J. An investigation of premixed flame propagation in a closed combustion duct with a 90° bend. Appl Energy 2014;134:248–56. https://doi.org/10.1016/j.apenergy.2014.07.071.
[43] Li Q, Sun X, Wang X, Zhang Z, Lu S, Wang C. Experimental study of flame propagation across flexible obstacles in a square cross-section channel. Int J Hydrogen Energy 2019;44:3944–52. https://doi.org/10.1016/j.ijhydene.2018.12.085.
[44] Bradley D, Harper CM. The development of instabilities in laminar explosion flames. Combust Flame 1994;99:562–72. https://doi.org/10.1016/0010-2180(94)90049-3.
[45] Bychkov V, Valiev D, Eriksson L-E. Physical mechanism of ultrafast flame acceleration. Phys Rev Lett 2008;101:164501. https://doi.org/10.1103/PhysRevLett.101.164501.
[46] McGarry JP, Ahmed KA. Flame–turbulence interaction of laminar premixed deflagrated flames. Combust Flame 2017;176:439–50. https://doi.org/10.1016/j.combustflame.2016.11.002.
[47] Han S, Yu M, Yang X, Wang X. Effects of obstacle position and hydrogen volume fraction on premixed syngas-air flame acceleration. Int J Hydrogen Energy 2020;45:29518–32. https://doi.org/10.1016/j.ijhydene.2020.07.189.

[48] Li Q, Ciccarelli G, Sun X, Lu S, Wang X, Zhang Z, et al. Flame propagation across a flexible obstacle in a square cross-section channel. Int J Hydrogen Energy 2018;43:17480–91. https://doi.org/10.1016/j.ijhydene.2018.07.077.

[49] di Sarli V, Benedetto A di. Sensitivity to the presence of the combustion submodel for large eddy simulation of transient premixed flame–vortex interactions. Ind Eng Chem Res 2012;51:7704–12. https://doi.org/10.1021/ie202061u.

[50] Sheng Z, Yang G, Gao W, Li S, Shen Q, Sun H. Study on the dynamic process of premixed hydrogen-air deflagration flame propagating in a closed space with obstacles. Fuel 2023;334:126542. https://doi.org/10.1016/j.fuel.2022.126542.